

Path-integral quantum Monte Carlo calculations of light nuclei

Rong Chen^{1,2,*} and Kevin E. Schmidt^{1,†}

¹*Department of Physics, Arizona State University, Tempe, Arizona 85287, USA*

²*Laboratory of Applied Pharmacokinetics and Bioinformatics, Children's Hospital Los Angeles, University of Southern California, Los Angeles, California 90027, USA*

(Dated: October 28, 2022)

We describe a path-integral ground-state quantum Monte Carlo method for light nuclei in continuous space. We show how to efficiently update and sample the paths with spin-isospin dependent and spin-orbit interactions. We apply the method to the triton and α particle using both local chiral interactions with next-to-next-to-leading-order and the Argonne interactions. For operators, like the total energy, that commute with the Hamiltonian, our results agree with Green's function Monte Carlo and auxiliary field diffusion Monte Carlo calculations. For operators that do not commute with the Hamiltonian and for Euclidean response functions, the path-integral formulation allows straightforward calculation without forward walking or the increased variance typical of diffusion methods. We demonstrate this by calculating density distributions, root-mean-square radii, and Euclidean response functions for single-nucleon couplings.

I. INTRODUCTION

Real space path-integral quantum Monte Carlo methods for calculating the properties of many-body systems with spin independent interactions [1–3], are often the methods of choice to calculate the ground-state expectation values of operators such as the one- and two-body density distributions, response functions, etc. that do not commute with the Hamiltonian.

Real-space nuclear quantum Monte Carlo calculations performed with diffusion Monte Carlo methods, such as Green's function Monte Carlo (GFMC) method [4] or the auxiliary field diffusion Monte Carlo (AFDMC) [5], sample the product of the ground-state wave function and the adjoint of a trial function. These methods can accurately calculate the ground-state energy and expectations of other operators that commute with the Hamiltonian using a mixed expectation value.

The calculation of other operators requires additional calculational steps, such as forward walking [6–8], in order to calculate their ground-state expectation. Forward walking methods typically have higher variance which can limit the length of the forward walked path and therefore the accuracy.

Many operators whose ground-state expectation is desired do not commute with the Hamiltonian. Two examples are the root-mean-square (RMS) radii and the particle number density. Additionally, calculating response functions where the system is propagated between the application of two operators require similar forward walking techniques with diffusion Monte Carlo methods.

Path-integral Monte Carlo (PIMC) methods [1, 2], on the other hand, sample and store the entire path. The energy calculation is typically more time consuming, however, the advantage is that the operators can be readily

inserted anywhere along the path. The ground-state expectation arbitrary operators or response functions is straightforwardly implemented.

In this paper we show how to implement a real-space path-integral method for realistic nuclear Hamiltonians. In order to give a proof of principle demonstration and investigate path sampling methods, we avoid the fermion sign or phase problem by looking at s-wave nuclei ($A \leq 4$) only, where the sign or phase problem is weak, and the calculations converge to their ground-state values before any substantial sign or phase problem manifests itself.

We use the local chiral interaction with next-to-next-to-leading-order [9–11] (N^2LO), and the Argonne v'_6 ($AV6'$) and v'_8 ($AV8'$) interactions [12]. We do not include three-body interactions, but they are straightforward to include in future calculations.

We calculate the ground-state energy, which can be directly compared with GFMC and AFDMC results [11, 12], and give path-integral results for the RMS radius, particle density distribution and several Euclidean response functions for single-nucleon couplings [13] whose operators do not commute with the Hamiltonian.

The paper is organized as follows. In Sec. II, we describe the framework for PIMC calculations. We introduce the Hamiltonian, the model space, the trial wave function, the short-time approximated propagator. We describe the error structure of our calculation which will be used to extrapolate to zero time step. In Sec. III, we describe the PIMC simulations and how to update the path efficiently. In Sec. IV, we investigate various Metropolis Monte Carlo sampling moves and strategies to sample the paths. In Sec. V we show results for the ground-state energy, RMS radii, single-particle number density and Euclidean response functions for single-nucleon couplings. Section VI gives a summary and outlook for possible future calculations.

* chen.rong@asu.edu; rongchen@chla.usc.edu

† kevin.schmidt@asu.edu

II. THEORETICAL FRAMEWORK

PIMC methods obtain the ground-state expectation value of a Hermitian operator \hat{O} using the matrix elements

$$\langle \hat{O} \rangle = \frac{\langle \Psi_T | e^{-H\tau_1} \hat{O} e^{-H\tau_2} | \Psi_T \rangle}{\langle \Psi_T | e^{-H\tau} | \Psi_T \rangle} \quad (1)$$

where τ_1 and τ_2 are imaginary times and the total imaginary time is $\tau = \tau_1 + \tau_2$. Ψ_T is a trial wave function which serves as the initial and final states of the path. $H = T + V$ is the Hamiltonian of the system where T and V are kinetic and potential energy operators.

For $\tau_1 = \tau_2 = 0$, the Eq.(1) is equivalent to a variational Monte Carlo calculation with trial state $|\Psi_T\rangle$.

For τ large enough, $e^{-H\tau}|\Psi_T\rangle$ projects out the ground state $|\Phi_0\rangle$, i.e., $\lim_{\tau \rightarrow \infty} e^{-H\tau}|\Psi_T\rangle \propto |\Phi_0\rangle$. So Eq.(1) becomes the ground-state expectation value of \hat{O} ,

$$\langle \hat{O} \rangle = \frac{\langle \Phi_0 | \hat{O} | \Phi_0 \rangle}{\langle \Phi_0 | \Phi_0 \rangle} \quad (2)$$

when τ_1 and τ_2 are large.

Mixed estimates, which are the exact ground-state expectations for the Hamiltonian and operators commute with the Hamiltonian, can be calculated by taking one of the τ_1 or τ_2 large and the other zero.

The propagator $e^{-H\tau_i}$ is sampled by writing

$$e^{-H\tau_i} = (e^{-H\Delta\tau})^{N_i} \quad (3)$$

and using a Trotter breakup of $e^{-H\Delta\tau}$ to approximate the short-time propagator.

In order to calculate the ground-state properties, we must use a sufficiently large τ_i such that $e^{-H\tau_i}$ can project out the ground state $|\Phi_0\rangle$. The time step $\Delta\tau$ is chosen small enough such that Trotter breakup errors can be either ignored or extrapolated out. A typical calculation is formulated as

$$\langle \hat{O} \rangle = \frac{\langle \Psi_T | e^{-H\Delta\tau} \dots e^{-H\Delta\tau} \hat{O} e^{-H\Delta\tau} \dots e^{-H\Delta\tau} | \Psi_T \rangle}{\langle \Psi_T | e^{-H\Delta\tau} \dots e^{-H\Delta\tau} e^{-H\Delta\tau} \dots e^{-H\Delta\tau} | \Psi_T \rangle} \quad (4)$$

Since T and V do not commute, the Trotter breakup for the short-time propagator $U(\Delta\tau)$ has a time-step error

$$U(\Delta\tau) = e^{-H\Delta\tau} + \mathcal{O}(\Delta\tau^k), \quad (5)$$

of order $\Delta\tau^k$. Different choices of $U(\Delta\tau)$ give different order for k .

Our calculations give $\langle \hat{O}(\Delta\tau) \rangle$, an approximation of the true expectation value $\langle \hat{O} \rangle$ in Eq.(4),

$$\langle \hat{O}(\Delta\tau) \rangle = \frac{\langle \Psi_T | [U(\Delta\tau)]^{N_1} \hat{O} [U(\Delta\tau)]^{N_2} | \Psi_T \rangle}{\langle \Psi_T | [U(\Delta\tau)]^{N_1+N_2} | \Psi_T \rangle} \quad (6)$$

In the limit where the time step $\Delta\tau$ becomes zero,

$$\lim_{\Delta\tau \rightarrow 0} \langle \hat{O}(\Delta\tau) \rangle = \langle \hat{O} \rangle. \quad (7)$$

To estimate the errors, we calculate $\langle \hat{O}(\Delta\tau) \rangle$ for different time step $\Delta\tau$ and extrapolate to $\Delta\tau = 0$ to find the true expectation value $\langle \hat{O} \rangle$. In Eqs.(4) and (6), for large-enough N_1 and N_2 , the numerator and denominator are real, and in the Monte Carlo results, we keep just the real part.

An advantage of PIMC is that since the entire path is sampled, it can directly deal with operators which do not commute with H , while diffusion-based methods like GFMC and AFDMC cannot do so without additional techniques such as forward walking [6]. As we can see from Eq.(4), a PIMC calculation depends on not only the operator \hat{O} , but also the Hamiltonian H , the trial wave function Ψ_T , and the short time propagator $e^{-H\Delta\tau}$. In the next sections we will describe each of these.

A. Hamiltonian

We choose the Hamiltonian H for our calculations to include just two-body potentials

$$H = \sum_{i=1}^A \frac{\mathbf{p}_i^2}{2m} + \sum_{i<j} V_{ij}, \quad (8)$$

where A is total number of nucleons in the system, in the position representation $\mathbf{p}_i = -i\hbar\nabla_i$, and $\frac{\hbar^2}{2m}$ is chosen as 20.375 fm². Since our PIMC calculation is a proof of principle benchmark test, we did not include three-body interaction in this work. The complete two-body interaction for a given ij pair of particles, V_{ij} , is composed of the nucleon-nucleon strong interaction V_{ij}^{NN} and the electromagnetic force V_{ij}^{EM} ,

$$V_{ij} = V_{ij}^{\text{NN}} + V_{ij}^{\text{EM}}. \quad (9)$$

We use the local chiral interaction with N²LO [9–11], the Argonne v'_6 (AV6') and v'_8 (AV8') interactions [12]. The nucleon-nucleon interaction can be written as,

$$V_{ij}^{\text{NN}} = \sum_{p=1}^8 v_p(r_{ij}) O_{ij}^p, \quad (10)$$

where r_{ij} is the length of \mathbf{r}_{ij} , $v_p(r_{ij})$ is the radial function for the p^{th} operator, with different functions for the chiral and Argonne interactions. The first six of the operators O_{ij}^p are the same for all the potentials we are using. They are 1, $\boldsymbol{\tau}_i \cdot \boldsymbol{\tau}_j$, $\boldsymbol{\sigma}_i \cdot \boldsymbol{\sigma}_j$, $\boldsymbol{\sigma}_i \cdot \boldsymbol{\sigma}_j \boldsymbol{\tau}_i \cdot \boldsymbol{\tau}_j$, S_{ij} and $S_{ij} \boldsymbol{\tau}_i \cdot \boldsymbol{\tau}_j$, where $\boldsymbol{\sigma}$ and $\boldsymbol{\tau}$ are spin and isospin operators and S_{ij} is the tensor force. The local chiral N²LO interaction has the additional seventh operator which is a spin-orbit term,

$$O_{ij}^7 = \mathbf{L} \cdot \mathbf{S}, \quad (11)$$

where \mathbf{L} is the relative angular momentum and \mathbf{S} is the total spin [11]. For the AV8' interaction, besides the first seven operators, it has the eighth operator which is a spin-orbit term coupled with the isospin term,

$$O_{ij}^8 = \mathbf{L} \cdot \mathbf{S} \boldsymbol{\tau}_i \cdot \boldsymbol{\tau}_j, \quad (12)$$

For the electromagnetic force V_{ij}^{EM} , here we just consider the Coulomb force term $v^{\text{C}}(r_{ij})$ between proton pairs.

B. Model space

The interaction used in this paper will not change Z , the total number of protons, so the number of possible isospin states is $\frac{A!}{Z!(A-Z)!}$. The tensor part S_{ij} can flip spins, so all 2^A spin states are allowed, giving $N_{\text{tot}} = \frac{A!}{Z!(A-Z)!} 2^A$ for the total number of spin-isospin basis states¹.

${}^4\text{He}$ then has $N_{\text{tot}} = 6 \times 16 = 96$ spin-isospin basis states. We write these basis states as $|S\rangle$ and S takes 96 values,

$$|S\rangle \equiv |s_1\rangle|s_2\rangle|s_3\rangle|s_4\rangle \equiv |s_1 s_2 s_3 s_4\rangle, \quad (13)$$

where s_i means the spin-isospin state of particle i , it can be any state from neutron spin up $|n \uparrow\rangle$, neutron spin down $|n \downarrow\rangle$, proton spin up $|p \uparrow\rangle$, and proton spin down $|p \downarrow\rangle$. We denote the spatial configuration of a system with A particles as R such that $R \equiv (\mathbf{r}_1, \mathbf{r}_2, \dots, \mathbf{r}_A)$, where $\mathbf{r}_i = (x_i, y_i, z_i)$ is the coordinates of particle i . The spatial configuration of ${}^4\text{He}$ can also be written as a state $|R\rangle$,

$$|R\rangle \equiv |\mathbf{r}_1\rangle|\mathbf{r}_2\rangle|\mathbf{r}_3\rangle|\mathbf{r}_4\rangle \equiv |\mathbf{r}_1 \mathbf{r}_2 \mathbf{r}_3 \mathbf{r}_4\rangle. \quad (14)$$

The basis states $|RS\rangle$ are

$$|RS\rangle = |R\rangle|S\rangle \equiv |\mathbf{r}_1 \mathbf{r}_2 \mathbf{r}_3 \mathbf{r}_4\rangle|s_1 s_2 s_3 s_4\rangle, \quad (15)$$

with the corresponding identity operators $\int dR |R\rangle\langle R| = 1$, $\sum_S |S\rangle\langle S| = 1$, and $\sum_S \int dR |RS\rangle\langle RS| = 1$.

If we ignore the Coulomb interaction, then the potentials conserve total isospin. Often GFMC calculations include the isospin breaking terms as a perturbation and work in a good total isospin basis, along with exploiting time-reversal invariance for the integer total spin case. This reduces the calculational basis size. We chose instead to include the isospin breaking interactions in the propagator and did not exploit time-reversal symmetry.

C. Wave function

We use a trial state $|\Psi_T\rangle$ of the form [15],

$$|\Psi_T\rangle = \mathcal{F}|\Phi\rangle = \mathcal{S} \prod_{i<j} F_{ij} |\Phi\rangle, \quad (16)$$

where $|\Phi\rangle$ is the model state, \mathcal{F} is the correlation operator which is a product of two-body correlation operators F_{ij} ,

$$F_{ij} = \sum_{p=1}^6 f_{ij}^p O_{ij}^p, \quad (17)$$

where O_{ij}^p are the AV6' operators and f_{ij}^p is the corresponding correlation function and \mathcal{S} is a symmetrization operator that acts only on the correlations to guarantee a properly antisymmetric state,

For $A \leq 4$, an s-wave model state can be constructed from a constant spatial function multiplying antisymmetric combinations of spin-isospin states and all spatial dependence is included as in Ref. [16]. We calculate the correlations by solving the two-body differential equations as described in Ref. [15] and Ref. [16] and adjust the parameters using the variational method. $|\Phi\rangle$ is chosen to have the correct quantum numbers for the desired state.

For $A \leq 4$, $|\Phi\rangle$ can be decomposed by a spatial part $|\Phi_R\rangle$ and a spin-isospin part $|\Phi_S\rangle$ such that

$$|\Phi\rangle = |\Phi_R\rangle|\Phi_S\rangle, \quad (18)$$

where $|\Phi_R\rangle$ is symmetrized which can be chosen as $|\Phi_R\rangle = \int dR |R\rangle$ such that $\langle R' | \Phi_R \rangle = \int dR \delta(R' - R) = 1$.

For example, for ${}^4\text{He}$, the spin-isospin model state is simply

$$|\Phi_S\rangle = \mathcal{A} |n \uparrow n \downarrow p \uparrow p \downarrow\rangle = \sum_{N=1}^{96} \phi_N |N\rangle. \quad (19)$$

\mathcal{A} is the antisymmetrization operator, and ϕ_N is either -1 or 1 depending on the antisymmetrization for each of the 24 basis states, and 0 for the rest 72 basis states. The wave function $\langle RS | \Phi \rangle$ becomes

$$\langle RS | \Phi \rangle = \sum_{N=1}^{96} \phi_N \langle S | N \rangle. \quad (20)$$

The trial wave function is

$$\langle RS | \Psi_T \rangle = \left\langle S \left| \mathcal{S} \prod_{i<j} \left[\sum_{p=1}^6 f_{ij}^p(r_{ij}) O_{ij}^p \right] \right| \Phi_S \right\rangle \quad (21)$$

where we sample the order of the correlations to apply the symmetrization operator \mathcal{S} as in Refs. [16] and [15]. We use a superscripts l and r on the states and products to denote a particular sampled order for the left and right trial functions of our path integral, $\langle \Psi_T^l |$ from $\langle \Psi_T |$ and $|\Psi_T^r\rangle$ from $|\Psi_T\rangle$ with

$$\langle \Psi_T | RS \rangle = \sum_l \langle \Psi_T^l | RS \rangle, \quad (22)$$

$$\langle RS | \Psi_T \rangle = \sum_r \langle RS | \Psi_T^r \rangle, \quad (23)$$

and

$$\langle RS | \Psi_T^r \rangle = \left\langle S \left| \prod_{i<j}^r \left[\sum_{p=1}^6 f_{ij}^p(r_{ij}) O_{ij}^p \right] \right| \Phi_S \right\rangle, \quad (24)$$

¹ In our PIMC code, the spin, isospin states are written using a binary representation [14], and we label the A particles from 0 to $A - 1$. The various Pauli matrix operators for the spin and isospin are implemented by bit flips and exchanges along with multiplication of the corresponding coefficients.

$$\langle \Psi_T^l | RS \rangle = \left\langle \Phi_S \left| \prod_{i < j} \left[\sum_{p=1}^6 f_{ij}^{p*}(r_{ij}) O_{ij}^p \right] \right| S \right\rangle. \quad (25)$$

D. Propagator

We write the free-particle propagator as

$$G_{R'R}^f = \langle R' | e^{-T\Delta\tau} | R \rangle = \left(\frac{m}{2\pi\Delta\tau\hbar^2} \right)^{\frac{3A}{2}} e^{-\frac{(R'-R)^2}{2\Delta\tau\frac{\hbar^2}{m}}}, \quad (26)$$

where $(R'-R)^2 = \sum_{i=1}^A (\mathbf{r}'_i - \mathbf{r}_i)^2$, and the potential part of the propagator, without the spin-orbit interaction, as

$$U_V(R, \frac{\Delta t}{2}) = e^{-\frac{\mathcal{V}_{A-1A}\Delta t}{2}} e^{-\frac{\mathcal{V}_{A-2A}\Delta t}{2}} \dots e^{-\frac{\mathcal{V}_{13}\Delta t}{2}} e^{-\frac{\mathcal{V}_{12}\Delta t}{2}} \quad (27)$$

where \mathcal{V}_{ij} contains the pair potential with the first six operators in Eq.(10) plus the electromagnetic force,

$$\mathcal{V}_{ij} = \sum_{p=1}^6 v_p(r_{ij}) O_{ij}^p + V_{ij}^{\text{EM}}(r_{ij}). \quad (28)$$

We choose a fixed order for the pair-potential exponentials. The operator $U_V^\dagger(R, \frac{\Delta t}{2})$ reverses the order of these exponentials. In the calculations, each of these exponentials is rewritten as $e^{-\sum_{p=1}^6 v_p(r_{ij}) O_{ij}^p \Delta\tau} = \sum_{p=1}^6 u_{ij}^p(r_{ij}) O_{ij}^p$, where we can solve for the coefficients $u_{ij}^p(r_{ij})$ given the r_{ij} .

Without a spin-orbit interaction, the short-time propagator is

$$\begin{aligned} & \langle R' S' | U(\Delta\tau) | RS \rangle \\ &= \left\langle S' \left| U_V^\dagger(R', \frac{\Delta t}{2}) U_V(R, \frac{\Delta t}{2}) \right| S \right\rangle G_{R'R}^f. \end{aligned} \quad (29)$$

Since the spin-orbit interaction is relatively weak, we include it at linear order in the time step. This avoids needing to include counter terms [15]. Operating the \mathbf{p}_j operators on the free-particle propagator replaces them

with $im\frac{(\mathbf{r}'_j - \mathbf{r}_j)}{\hbar\Delta\tau}$. The short-time propagator with spin-orbit interactions becomes

$$\begin{aligned} & \langle R' S' | U(\Delta\tau) | RS \rangle \\ &= \langle S' | U_V^\dagger(R', \frac{\Delta\tau}{2}) \mathcal{G}(R', R) U_V(R, \frac{\Delta\tau}{2}) | S \rangle G_{R'R}^f, \end{aligned} \quad (30)$$

with

$$\begin{aligned} \mathcal{G}(R', R) &= 1 + \frac{m}{4i\hbar^2} \sum_{i < j} [v_7(r'_{ij}) + v_8(r'_{ij}) \boldsymbol{\tau}_i \cdot \boldsymbol{\tau}_j] \cdot \\ & \left[\mathbf{r}'_{ij} \times \Delta \mathbf{r}_{ij}^{R', R} \cdot (\boldsymbol{\sigma}_i + \boldsymbol{\sigma}_j) \right], \end{aligned} \quad (31)$$

where r'_{ij} is the distance between particle i and j in configuration R' , $\mathbf{r}'_{ij} \equiv \mathbf{r}_i - \mathbf{r}_j$ in R' , $\Delta \mathbf{r}_{ij}^{R', R} \equiv \Delta \mathbf{r}_i^{R', R} - \Delta \mathbf{r}_j^{R', R}$ where $\Delta \mathbf{r}_{i(j)}^{R', R} \equiv \mathbf{r}_{i(j)}^{R'} - \mathbf{r}_{i(j)}^R$, and the symbol $\mathbf{r}_{i(j)}^R$ means the $\mathbf{r}_{i(j)}$ in configuration R .

E. Error estimation

We use the $U(\Delta\tau)$ in Eq.(30) as the short-time propagator for local chiral N²LO interaction and the AV8' interaction. It gives a time-step error for the path which is linear in the time step. We fit the coefficient C_1 to this error for short times,

$$\langle \hat{O}(\Delta\tau) \rangle = \langle \hat{O} \rangle + C_1(\Delta\tau), \quad (32)$$

to extrapolate to the zero time-step limit.

For AV6' we use $U(\Delta\tau)$ in Eq.(29) and we can immediately find in this case $U(\Delta\tau)U(-\Delta\tau) = 1$. The difference between $e^{-H\Delta\tau}$ and $U(\Delta\tau)$ only contains odd order terms in $\Delta\tau$ [17, 18]. The time-step error in the full path is extrapolated to zero by fitting to

$$\langle \hat{O}(\Delta\tau) \rangle = \langle \hat{O} \rangle + C_2(\Delta\tau^2). \quad (33)$$

III. PATH-INTEGRAL FORM

We write Eq.(6) in a form suitable for Monte Carlo calculations. The total time $\tau = \tau_1 + \tau_2 = N\Delta\tau$, with $\Delta\tau$ the time step. The path integral becomes

$$\langle \hat{O}(\Delta\tau) \rangle = \frac{\text{Re} \sum_{S_0, S_N} \int \mathcal{D}\mathcal{R} \langle \Psi_T | R_0 S_0 \rangle \langle R_0 S_0 | [U(\Delta\tau)]^{N_1} \hat{O} [U(\Delta\tau)]^{N_2} | R_N S_N \rangle \langle R_N S_N | \Psi_T \rangle}{\text{Re} \sum_{S_0, S_N} \int \mathcal{D}\mathcal{R} \langle \Psi_T | R_0 S_0 \rangle \langle R_0 S_0 | [U(\Delta\tau)]^N | R_N S_N \rangle \langle R_N S_N | \Psi_T \rangle}, \quad (34)$$

where we assume that the times are long enough to make the numerator and denominator real, as noted above, and take the real parts in the Monte Carlo calculations. The symbol \mathcal{R} denotes all of the spatial configurations

$\{R_0, R_1, \dots, R_N\}$, and we call each of the R_I a bead. The integral of \mathcal{R} is the spatial integral over all the configurations R_I , i.e., $\int \mathcal{D}\mathcal{R} \equiv \prod_{I=0}^N \int dR_I$.

In addition to the position integrals, since we sample

the order of the operators in the trial functions, we write the sampled left and right orders as l and r , as in Eqs. (22) and (23). Eq. (34) is then in the form

$$\begin{aligned} \langle \hat{O}(\Delta\tau) \rangle &= \frac{\sum_l \sum_r \int \mathcal{D}\mathcal{R} A_{lr}(\mathcal{R}) P_{lr}(\mathcal{R})}{\sum_l \sum_r \int \mathcal{D}\mathcal{R} B_{lr}(\mathcal{R}) P_{lr}(\mathcal{R})} \\ &= \frac{\langle A_{lr}(\mathcal{R}) \rangle}{\langle B_{lr}(\mathcal{R}) \rangle} \Big|_{\{l,r,\mathcal{R}\} \in P_{lr}(\mathcal{R})}. \end{aligned} \quad (35)$$

In Eq.(35), the $A_{lr}(\mathcal{R})$ and $B_{lr}(\mathcal{R})$ are real functions which can be written as $A_{lr}(\mathcal{R}) = \frac{\text{Re}[g_{lr,M}^V(\mathcal{R})]}{|\text{Re}[f_{lr}^V(\mathcal{R})]|}$ and $B_{lr}(\mathcal{R}) = \frac{\text{Re}[f_{lr}^V(\mathcal{R})]}{|\text{Re}[f_{lr}^V(\mathcal{R})]|}$, with $B_{lr}(\mathcal{R})$ either 1 or -1 indicating the weak sign problem for the $A \leq 4$ nuclei. $P_{lr}(\mathcal{R})$ is the normalized probability distribution,

$$P_{lr}(\mathcal{R}) = \frac{|\text{Re}[f_{lr}^V(\mathcal{R})g^F(\mathcal{R})]|}{\mathcal{N}}, \quad (36)$$

with $\sum_l \sum_r \int d\mathcal{R} P_{lr}(\mathcal{R}) = 1$. As usual, the normalization factor \mathcal{N} cancels in the Metropolis algorithm implementation.

The detailed forms and calculations of the functions $g^F(\mathcal{R})$, $g_{lr,M}^V(\mathcal{R})$, and $f_{lr}^V(\mathcal{R})$ are presented in Eqs. (A6), (A13), and (A15) in Appendix. A which describes how the path is calculated. The calculations of the path updating is presented in Appendix. B. More details can be found in Chapter 2 in Ref. [19].

With Eq.(6) written in the form of Eq. (35), it can now be calculated by sampling the probability distribution $P_{lr}(\mathcal{R})$, and averaging the numerator and denominator $A_{lr}(\mathcal{R})$ and $B_{lr}(\mathcal{R})$ in Eq.(35), along with the statistical errors.

IV. MONTE CARLO SAMPLING

Our PIMC is based on the standard Metropolis method [1, 20, 21]. We calculate $\langle F \rangle$, the expectation value of the function $F(s)$, as

$$\langle F \rangle = \sum_s F(s) \pi(s), \quad (37)$$

where $\pi(s)$ is a normalized probability distribution such that $\sum_s \pi(s) = 1$; it describes the probability for state s to occur, where s represents the set of sampled variables. In the standard Metropolis method we propose a transition from the state s to a new state s' with probability $T(s \rightarrow s')$. We accept the new state with the Metropolis probability

$$A(s \rightarrow s') = \min \left[1, \frac{\pi(s')T(s' \rightarrow s)}{\pi(s)T(s \rightarrow s')} \right], \quad (38)$$

satisfying detailed balance. Below we will describe several transition probabilities that we have used to implement an efficient path integral sampling for the nuclear problem.

A. Metropolis method in PIMC

We take $\pi(s)$ in Eq.(37) to be $P_{lr}(\mathcal{R})$ in Eq.(36). The state s is then a particular choice of the left and right correlation operator orders in the trial function and the bead positions that describe the path $\{l, r, \mathcal{R}\}$.

We separately sample the left and right trial wave-function correlation operator order and the bead positions.

For the sampling of the operator orders in the trial wave function, we write

$$T(s \rightarrow s') = T_{lr \rightarrow l'r'}. \quad (39)$$

We randomly choose new permutations of the orders, so $T_{lr \rightarrow l'r'}$ and $T_{l'r' \rightarrow lr}$ are equal and the acceptance probability is

$$A(s \rightarrow s') = \min \left[1, \frac{f_{l'r'}^V(\mathcal{R})g^F(\mathcal{R})}{f_{lr}^V(\mathcal{R})g^F(\mathcal{R})} \right]. \quad (40)$$

Since only the ordering of the trial wave-function correlations changes, these calculations are independent of the length of the path. Since the commutators of the correlations are typically small, these moves are usually accepted.

We propose new beads positions \mathcal{R}' with the transition probability

$$T(s \rightarrow s') = T_{lr}(\mathcal{R} \rightarrow \mathcal{R}'), \quad (41)$$

where $T_{lr}(\mathcal{R} \rightarrow \mathcal{R}')$ samples the new positions \mathcal{R}' for the path beads, given the new accepted order lr . We use several different methods described below to efficiently sample the paths.

B. Multilevel sampling

We write the proposed transition probability $T_{lr}(\mathcal{R} \rightarrow \mathcal{R}')$ and $T_{lr}(\mathcal{R}' \rightarrow \mathcal{R})$ in Sec IV A in a way such that,

$$g^F(\mathcal{R}')T_{lr}(\mathcal{R}' \rightarrow \mathcal{R}) = g^F(\mathcal{R})T_{lr}(\mathcal{R} \rightarrow \mathcal{R}'), \quad (42)$$

and the corresponding acceptance rate becomes,

$$A(s \rightarrow s') = \min \left[1, \frac{f_{lr}^V(\mathcal{R}')}{f_{lr}^V(\mathcal{R})} \right]. \quad (43)$$

We use the Gaussian propagators in $g^F(\mathcal{R}')$ to sample such a new proposed free-particle path \mathcal{R}' . There are many ways to do this. Here, since we wished to test the implementation of the bisection method [1] commonly used for central hard-core interactions, we sample the points using what we call multilevel sampling.

From the total $N + 1$ beads on the imaginary time from bead 0 to bead N , we randomly pick $2^n + 1$ consecutive beads from bead I to bead $I + 2^n$, where n is a positive

integer. Here we refer to these beads from bead I to bead $I + 2^n$ as R_0 to R_{2^n} , with configurations represented by

$$\mathcal{R} = \{R_0, R_1, R_2, \dots, R_{2^n-1}, R_{2^n}\}. \quad (44)$$

We keep R_0 and R_{2^n} unchanged and propose the new configurations for the beads in between them. The relevant new proposed beads at each level are,

$$\begin{aligned} \text{Level 0 : } & R_0, R_{2^n}. \\ \text{Level 1 : } & R'_{\frac{1}{2}2^n}. \\ \text{Level 2 : } & R'_{\frac{1}{4}2^n}, R'_{\frac{3}{4}2^n}. \\ & \vdots \\ \text{Level } k : & R'_{\frac{1}{2^k}2^n}, R'_{\frac{3}{2^k}2^n}, \dots, R'_{\frac{2^k-1}{2^k}2^n}. \\ & \vdots \\ \text{Level } n : & R'_1, R'_2, \dots, R'_{2^n-1}. \end{aligned}$$

We denote bead M as the bead located in the middle of bead L and bead N . We propose the new beads R'_M at each level according to the average position of R'_L and R'_N from the previous level, plus a random Gaussian number vector \mathbf{g} whose standard deviation at each dimension is $\sigma = \sqrt{\frac{|N-L|}{2} \Delta\tau \frac{\hbar^2}{2m}}$ and average is zero,

$$R'_M = \frac{R'_L + R'_N}{2} + \mathbf{g}. \quad (45)$$

In this way, we are actually setting the proposed transition probability $T_{lr}(\mathcal{R} \rightarrow \mathcal{R}')$ as,

$$T_{lr}(\mathcal{R} \rightarrow \mathcal{R}') = g^F(\mathcal{R}'). \quad (46)$$

This satisfies Eq.(42) and we can use Eq.(43) for the acceptance probability.

To calculate $f_{lr}^V(\mathcal{R}')/f_{lr}^V(\mathcal{R})$, we define states $|\psi_M^r(\mathcal{R})\rangle$ and $|\psi_M^l(\mathcal{R})\rangle$ as shown in Eqs. (B1) and (B2) in Appendix B, as well as the corresponding probability amplitude. $\phi_M^r(\mathcal{R}, S)$ and $\phi_M^l(\mathcal{R}, S)$, as shown in Eqs. (A11) and (A12) in Appendix A. When we propose new moves from bead $I + 1$ to bead $I + 2^n - 1$, we calculate from $\phi_{I+2^n-1}^r(\mathcal{R}', S)$ to $\phi_{I+1}^r(\mathcal{R}', S)$, using the recursion relations Eq. (B1) starting from our previously calculated $\phi_{I+2^n}^r(\mathcal{R}, S)$. From this we use Eq. (A15) to calculate $f_{lr}^V(\mathcal{R}') = \langle \psi_I^l(\mathcal{R}') | \mathcal{G}(\mathcal{R}'_I, \mathcal{R}'_{I+1}) | \psi_{I+1}^r(\mathcal{R}') \rangle$, and with the previously calculated $f_{lr}^V(\mathcal{R})$ find $f_{lr}^V(\mathcal{R}')/f_{lr}^V(\mathcal{R})$. If the proposed move is accepted, then we update the rest of the beads. From right to left we update from $\phi_I^r(\mathcal{R}', S)$ until $\phi_0^r(\mathcal{R}', S)$, and from left to right we update from $\phi_{I+1}^r(\mathcal{R}', S)$ until $\phi_N^r(\mathcal{R}', S)$.

We choose the number of beads to optimize the time for these moves. Since updating is relatively expensive, we choose the number of beads to obtain a relatively small acceptance rate as discussed later.

C. Bead sampling

In order to make the total PIMC algorithm more robust, we can occasionally add a variety of other moves in addition to multilevel sampling alone in order to ensure an independent sampling of the path.

We randomly select a set of beads. In these beads we move the constituent particles with a displacement, either uniformly in a cube or with a Gaussian distribution, around their current position. As expected either sampling method gives a comparable acceptance.

We also tried moves where we translated all of the particles in all of the beads by the same $3A$ -dimensional random vector Λ , i.e.,

$$R'_I = R_I + \Lambda, \quad (47)$$

which we call a shift.

D. Sampling strategies

Besides the sampling methods described this section, we also tested using the bisection method [1] and reptation Monte Carlo method [3, 22] generalized to spin/isospin dependence.

The proposed trial moves at each level in multilevel sampling are the same as bisection method [1]. The advantage of the bisection method is that moves where the middle bead of the path is sampled in region where the potential is highly repulsive, and therefore likely to be rejected, are rejected early to minimize computations. We tried bisection but found that with these softer nuclear potentials with spin/isospin dependence, the approximate path values when the first intermediate beads was sampled, was not a particularly good predictor of the final path's value. Early rejection of the path did not give a more efficient method. Therefore our acceptance probability is based only on the entire path and there is only a single accept-reject step after the entire path is constructed.

The reptation method samples the spatial configuration of the path by adding some beads at one end of the path and removing some beads to the other end of the path. However, since we have spin and isospin sums in the path calculation, removing and adding beads, even if just one bead is involved, requires the recalculation of the whole path. Therefore, after initial testing, we did not pursue reptation moves; they are not efficient here.

For multilevel sampling, for the total $N + 1$ beads along the path, we pick two lengths of sets of beads: $n_1 \approx N/3$ and $n_2 \approx N/6$. About 80% of the moves are proposed for n_1 beads and the others are for n_2 beads. The acceptance rate for n_1 beads sampling is about 20% and for n_2 beads is about 40%. The n_2 beads case are mainly used for sampling the beads including the 0th and the N th beads.

The bead sampling methods discussed above are included but are not performed as often since they are not as efficient as the multilevel sampling.

About 90% of the moves use multilevel sampling and the other 10% are proposed by different kinds of bead sampling, which include moving beads one by one, moving all the beads at the same time, and a shift of all the beads at the same time, as described in Sec. IV C.

V. RESULTS AND DISCUSSIONS

We have calculated the ground-state energy, density distribution, root-mean-square radii, and Euclidean response functions for single-nucleon couplings. The detailed expressions such as the $g_{lr,M}^V(\mathcal{R})$ for each of these quantities can be found in Ref. [19].

A. Ground-state energy

The calculation of the ground-state energy E_0 can be written in the form of Eq.(35) as discussed in Sec. III, with the operator \hat{O} being the Hamiltonian. As indicated by Eq. (A14), we calculate the ground-state energy E_0 using

$$E_0 = \frac{\frac{1}{2} \text{Re} \langle \Psi_T | H e^{-H\tau} | \Psi_T \rangle + \langle \Psi_T | e^{-H\tau} H | \Psi_T \rangle}{\text{Re} \langle \Psi_T | e^{-H\tau} | \Psi_T \rangle}. \quad (48)$$

We conclude that $\tau = 0.1 \text{ MeV}^{-1}$ is sufficient to remove excited states and project out the ground state, by considering the energy gap to the excited states of about 20 MeV, along with the variational bound of about -23 MeV with our trial wave function. Since most operators will be placed in the middle of the path, we conclude the total imaginary time needs to be about $\tau = 0.2 \text{ MeV}^{-1}$ for convergence.

In Fig. 1 we show the α particle energy versus time step for each potentials studied. Figure 1 combines Fig. 2, 3, and 4 together, so it is visually easy to see the differences among the ground-state energies predicted by AV6', local N²LO, and AV8' interactions.

In Fig. 2, we show the AV6' results for the ⁴He ground state energy E_0 for different total imaginary time. As pointed out in Eq. (33), for AV6', our PIMC results should contain $\Delta\tau^2$ order error. In order to do extrapolation using Eq.(33), we need to find the range of $\Delta\tau$ where the error of $\Delta\tau^2$ dominates. Roughly, by looking at Eq.(33) we would require $|\frac{C_2\Delta\tau^2}{C_4\Delta\tau^4}| \gg 1$ where C_4 is the coefficient for the possible $\Delta\tau^4$ order term. From an analysis of the neglected commutator terms we expect $\Delta\tau$ to be around $10^{-4} - 10^{-3} \text{ MeV}^{-1}$. In Fig. 2 we can observe a clear $\Delta\tau^2$ dependence when $\Delta\tau < 1.3 \times 10^{-3} \text{ MeV}^{-1}$, and by using Eq.(33), the true ground-state energy E_0 is extrapolated to $-26.16(1) \text{ MeV}$. This is consistent with the GFMC result [12] of $E_0 = -26.15(2) \text{ MeV}$, as expected.

In Fig. 3 we show the results of ⁴He based on the local chiral N²LO two-body interaction with a coordinate space cutoff [9, 23] of $R_0 = 1.2 \text{ fm}$. As discussed in Sec. II D and

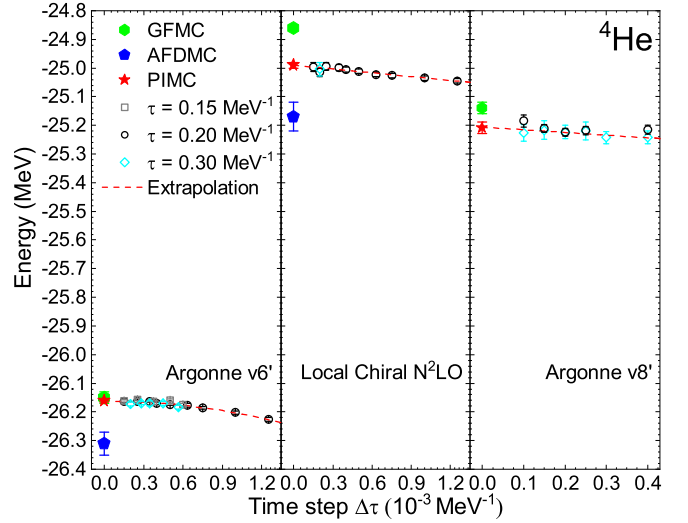


FIG. 1. Energy vs. time step $\Delta\tau$ for different total imaginary time τ for ⁴He based on AV6', local chiral N²LO, and AV8' interactions. For the extrapolated ground-state energy at $\Delta\tau = 0 \text{ MeV}^{-1}$ for GFMC and PIMC, the size of each symbols represents the corresponding error bar.

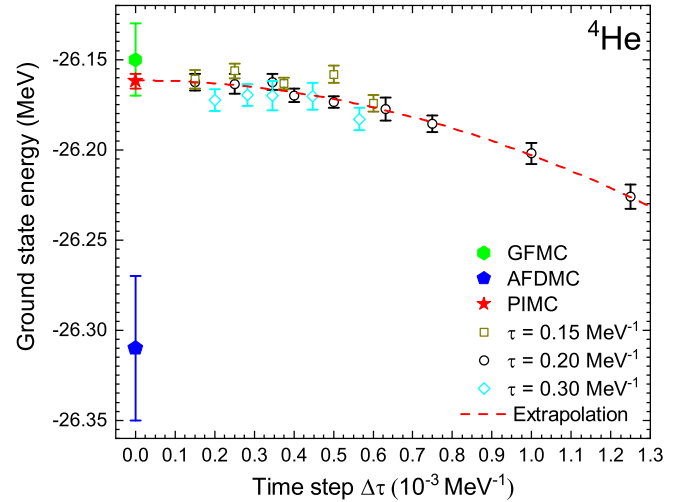


FIG. 2. Energy vs. time step $\Delta\tau$ for different total imaginary time τ for ⁴He based on AV6' interaction. The PIMC quadratic extrapolation is based on $\tau = 0.2 \text{ MeV}^{-1}$. The ground-state energy is extrapolated to $-26.162(4) \text{ MeV}$.

Eq.(32), due to our approximations in handling the spin-orbit operator, the lowest-order time-step error will be order $\Delta\tau$. In the same $\Delta\tau < 1.3 \times 10^{-3} \text{ MeV}^{-1}$ range as AV6', we do observe the $\Delta\tau$ error dominates as indicated in Eq.(32) and the extrapolated ground-state energy is $E_0 = -24.99(1) \text{ MeV}$.

In Fig. 4 the results of ⁴He based on AV8' interaction are presented. Due to our approximations in handling the spin-orbit terms, as in the local chiral N²LO interaction case, the time-step error is order $\Delta\tau$ as shown in Eq.(32). The linear extrapolation range of the time step is found

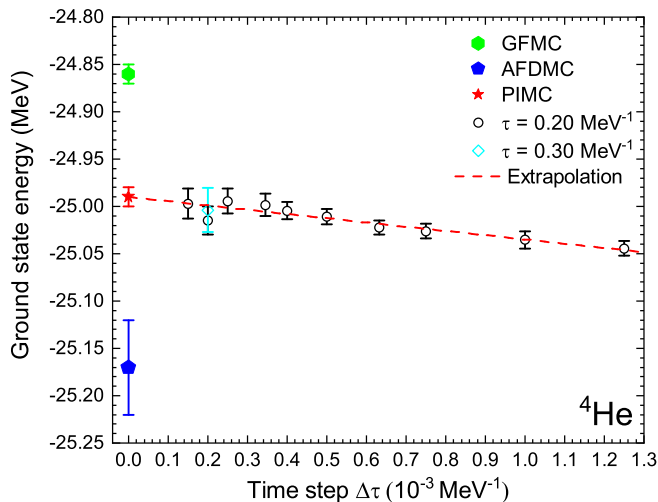


FIG. 3. Energy vs. time step $\Delta\tau$ for different total imaginary time τ for ${}^4\text{He}$ based on local chiral N^2LO interaction. The PIMC linear extrapolation is based on $\tau = 0.2 \text{ MeV}^{-1}$. The ground-state energy is extrapolated to $-24.99(1) \text{ MeV}$.

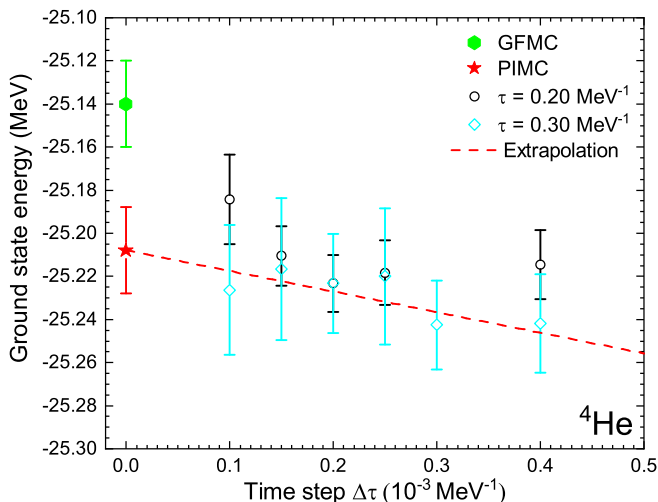


FIG. 4. Energy vs. time step $\Delta\tau$ for different total imaginary time τ for ${}^4\text{He}$ based on $\text{AV8}'$ interaction. The PIMC linear extrapolation is based on $\tau = 0.3 \text{ MeV}^{-1}$. The ground-state energy is extrapolated to $-25.21(2) \text{ MeV}$.

to be $\Delta\tau < 0.4 \times 10^{-3} \text{ MeV}^{-1}$, and the extrapolated ground-state energy is $E_0 = -25.21(2) \text{ MeV}$.

TABLE I. The ground-state energy of light nuclei based on the $\text{AV6}'$ interaction.

${}^A Z$	E_0 (MeV)	τ (MeV^{-1})	E_0^{GFMC} (MeV)	E_0^{EXPT} (MeV)
${}^2\text{H}$	-2.24(4)	0.5		-2.22
${}^3\text{H}$	-7.953(5)	0.4	-7.95(1)	-8.48
${}^3\text{He}$	-7.336(6)	0.5		-7.72
${}^4\text{He}$	-26.162(4)	0.2	-26.15(2)	-28.30

TABLE II. The ground-state energy of light nuclei based on the local chiral N^2LO interaction.

${}^A Z$	E_0 (MeV)	τ (MeV^{-1})	E_0^{GFMC} (MeV)	E_0^{AFDMC} (MeV)
${}^2\text{H}$	-2.20(1)	0.5	-2.20	
${}^3\text{H}$	-7.74(1)	0.4	-7.74(1)	-7.76(3)
${}^3\text{He}$	-7.11(1)	0.5	-7.01(1)	-7.12(3)
${}^4\text{He}$	-24.99(1)	0.2	-24.86(1)	-25.17(5)

TABLE III. The ground-state energy of light nuclei based on the $\text{AV8}'$ interaction.

${}^A Z$	E_0 (MeV)	τ (MeV^{-1})	E_0^{GFMC} (MeV)	E_0^{AFDMC} (MeV)
${}^2\text{H}$	-2.24(1)	0.5		
${}^3\text{H}$	-7.79(2)	0.4	-7.76(1)	
${}^3\text{He}$	-7.17(4)	0.5		
${}^4\text{He}$	-25.21(2)	0.3	-25.14(2)	

The ground-state energy for all the $A \leq 4$ nuclei are listed in Table I for the $\text{AV6}'$ interaction², in Table II for the chiral N^2LO interaction, and in Table III for $\text{AV8}'$ interaction. The GFMC and AFDMC results [11, 23] are listed for comparison. Overall, all the PIMC, GFMC, and AFDMC results are consistent with each other within 1% error. We also listed E_0^{EXPT} as the experimental value of the binding energies [12, 24, 25] for comparison. The difference between the experimental values and our results is mainly due to the absence of the three-body interactions in our calculations.

To confirm our conclusion that $\tau = 0.2 \text{ MeV}^{-1}$ for $\text{AV6}'$ and the chiral N^2LO , as well as $\tau = 0.3 \text{ MeV}^{-1}$ for $\text{AV8}'$ interactions are sufficient to project to the ground state, we calculate the potential energy $V = V^{\text{NN}} + V^{\text{EM}}$ along all the beads on the path. The calculation is done in the same way as in Sec. III. We use the potential operator V as the operator \hat{O} , and we place the V at each imaginary time position from bead 0 to the last bead N on the path to calculate $\langle V(\tau_1) \rangle$,

$$\langle V(\tau_1) \rangle = \frac{\text{Re} \langle \Psi_T | e^{-H\tau_1} V e^{-H(\tau-\tau_1)} | \Psi_T \rangle}{\text{Re} \langle \Psi_T | e^{-H\tau} | \Psi_T \rangle}, \quad (49)$$

where τ_1 ranges from 0 MeV^{-1} to τ as we put the V operator from bead 0 to bead N . $\langle V(\tau_1) \rangle$ is symmetric around $\tau_1 = \tau/2$. When $\tau/2$ is big enough to project out the ground state, $\langle V(\tau/2) \rangle$ is the ground-state potential energy.

In Fig. 5, in the upper panel we show the results for $\langle V(\tau_1) \rangle$ as a function of τ_1 for $\tau = 0.2 \text{ MeV}^{-1}$. The different curves are calculations with different time steps, that is, different numbers of beads. We see the result converges within error bars when $\Delta\tau \leq 2.5 \times 10^{-4} \text{ MeV}^{-1}$. Since the potential is more sensitive to first-order errors in

² In all tables we leave the entry blank if there is no data available.

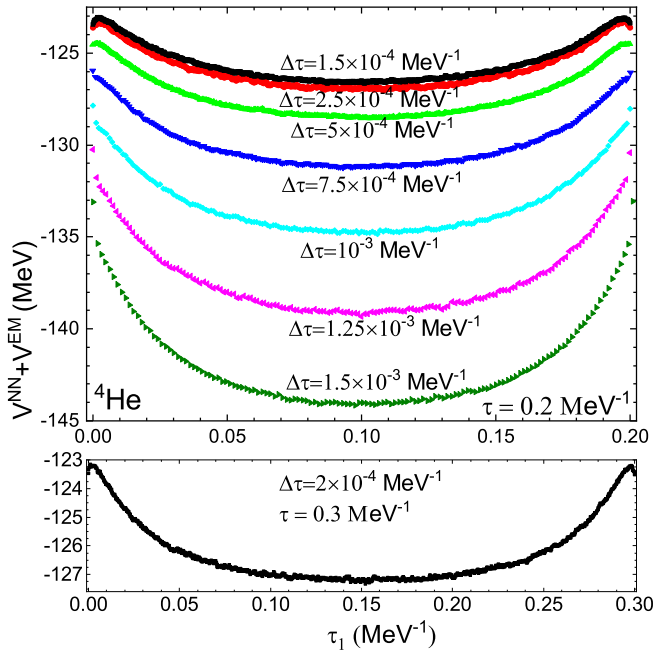


FIG. 5. The potential energy along the beads for $\tau = 0.2 \text{ MeV}^{-1}$ and $\tau = 0.3 \text{ MeV}^{-1}$ for ${}^4\text{He}$ based on the AV6' interaction. The error bar of the potential energy at each point is not plotted since it is smaller than the size of the corresponding symbol.

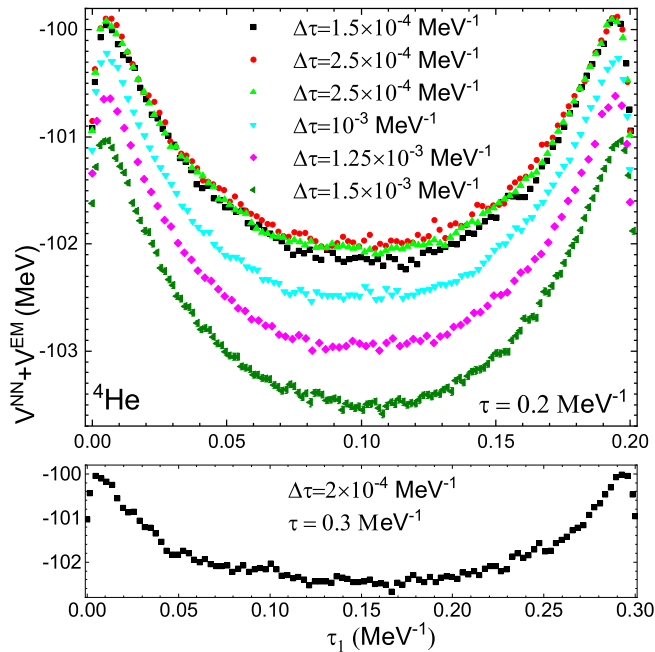


FIG. 6. The potential energy along the beads for $\tau = 0.2$ and 0.3 MeV^{-1} for ${}^4\text{He}$ based on the local chiral N^2LO interaction. From top to bottom, the $\Delta\tau$ corresponding to each of the plot is displayed. The error bar of the potential energy at each point is equal to or smaller than the size of the corresponding symbol.

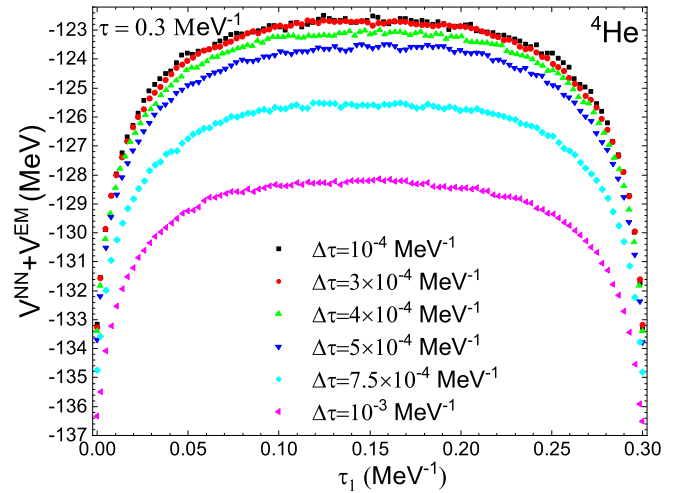


FIG. 7. The potential energy along the beads for $\tau = 0.3 \text{ MeV}^{-1}$ for ${}^4\text{He}$ based on the AV8' interaction. From top to bottom, the $\Delta\tau$ corresponding to each of the plot is displayed. The error bar of the potential energy at each point is equal to or smaller than the size of the corresponding symbol.

the wave function, we verify that the path is long enough for convergence to the ground state by calculating with a total $\tau = 0.3 \text{ MeV}^{-1}$ in the lower panel. We see that the central region is essentially flat and in agreement with the $\tau = 0.2 \text{ MeV}^{-1}$ central points.

Figure 6 is a similar graph for the local chiral interaction which also indicates $\tau = 0.2 \text{ MeV}^{-1}$ is sufficient. Figure 7 shows $\tau = 0.3 \text{ MeV}^{-1}$ for AV8' interactions is sufficient.³

B. Root-mean-square radii

The RMS radius r_m is the square root of the expectation value of the operator

$$\widehat{r}_m^2 = \frac{1}{A} \sum_{i=1}^A \left| \hat{r}_i - \frac{1}{A} \sum_{j=1}^A \hat{r}_j \right|^2. \quad (50)$$

We similarly define these RMS radii separately for the protons and neutrons by including isospin projection operators. Since the RMS radii operators do not commute with H , they require forward walking to calculate them using diffusion-based methods. In PIMC, they can be calculated directly.

³ In order to save computation time, we did not include spin-orbit interaction in the plot, but it does not alter the conclusion. Figure 6 is not as smooth as Fig. 5 because we ran the calculation for less time with somewhat higher statistical errors.

TABLE IV. PIMC results for RMS radii of light nuclei based on AV6' interaction.

${}^A Z$	r_m (fm)	r_p (fm)	r_n (fm)
${}^2\text{H}$	1.98(2)		
${}^3\text{H}$	1.7261(5)	1.6240(4)	1.7751(5)
${}^3\text{He}$	1.7426(6)	1.7962(6)	1.6289(5)
${}^4\text{He}$	1.4716(2)	1.4736(2)	1.4693(2)

TABLE V. PIMC results for RMS radii of light nuclei based on local chiral N²LO interaction.

${}^A Z$	r_m (fm)	r_p (fm)	r_n (fm)
${}^2\text{H}$	1.991(1)		
${}^3\text{H}$	1.7497(7)	1.6430(6)	1.8007(7)
${}^3\text{He}$	1.7725(8)	1.8292(9)	1.6520(7)
${}^4\text{He}$	1.4860(4)	1.4882(4)	1.4834(4)

TABLE VI. PIMC results for RMS radii of light nuclei based on AV8' interaction.

${}^A Z$	r_m (fm)	r_p (fm)	r_n (fm)
${}^2\text{H}$	1.965(3)		
${}^3\text{H}$	1.760(1)	1.653(1)	1.811(1)
${}^3\text{He}$	1.784(2)	1.841(2)	1.665(2)
${}^4\text{He}$	1.486(1)	1.488(1)	1.483(1)

In Tables IV, V, and VI, we list PIMC ground-state nucleon RMS radii based on the AV6', N²LO local chiral, and AV8' interactions. For ${}^2\text{H}$, since there is no Coulomb interaction, $r_m = r_p = r_n$. For other nuclei, however, due to the isospin dependent NN interaction part in the NN interaction) and the Coulomb interaction, r_m , r_p and r_n are, of course, not the same. Our results are in agreement with those in Ref. [23].

C. Density distribution

The single-particle number density $\rho(r)$ gives the probability density for one particle to be at distance r from the nuclei's center of mass [26]. We normalize so that $\int 4\pi r^2 \rho(r) dr = 1$, with

$$\hat{\rho}(r) = \frac{1}{A4\pi r^2} \sum_{i=1}^A \delta \left(r - \left| \hat{\mathbf{r}}_i - \frac{1}{A} \sum_{j=1}^A \hat{\mathbf{r}}_j \right| \right). \quad (51)$$

We further define the corresponding proton and neutron operators as

$$\hat{\rho}_{p(n)}(r) = \frac{1}{A4\pi r^2} \sum_{i=1}^A \delta \left(r - \left| \hat{\mathbf{r}}_i - \frac{1}{A} \sum_{j=1}^A \hat{\mathbf{r}}_j \right| \right) P_{p(n)}^i, \quad (52)$$

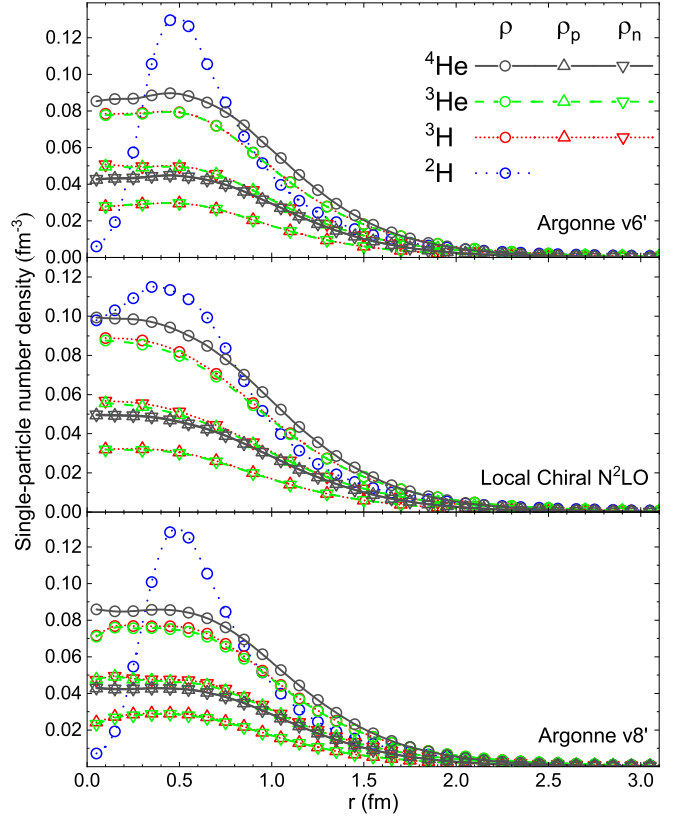


FIG. 8. The ground-state one-particle number density distributions of $A \leq 4$ light nuclei based on the AV6', local chiral N²LO, and AV8' interactions. The lines are a guide to the eye. ρ_p and ρ_n are equal to $\rho/2$. The error bar of one-particle number density at each point is not plotted since it is much smaller than the size of the corresponding symbol.

where $P_p^i = \frac{1+\tau_{iz}}{2}$ and $P_n^i = \frac{1-\tau_{iz}}{2}$ are the proton and neutron projection operator for nucleon with label i . Since $P_p^i + P_n^i = 1$, we have $\hat{\rho}(r) = \hat{\rho}_p(r) + \hat{\rho}_n(r)$. The number density operators do not commute with H , but again, in PIMC, they can be calculated directly.

In Fig. 8 all the density distributions for $A \leq 4$ light nuclei are presented.

D. Response functions

Euclidian response functions[13, 27–30] which, in principle, can be analytically continued to real time, open up the possibility of exploring the effects of scattering and other interactions with nuclei. Again, the related operators do not commute with H . So using PIMC is a natural method to use to calculate response functions. In an electron-nucleus scattering experiment, the response of a weakly coupled external probe can be written as the dynamic structure factor response function $S(k, \omega)$ which

can be expanded in the energy eigenstates [13], as

$$S(k, \omega) = \frac{\sum_n \langle \Phi_0 | \rho^\dagger(\mathbf{k}) | \Phi_n \rangle \langle \Phi_n | \rho(\mathbf{k}) | \Phi_0 \rangle \delta(\omega + E_0 - E_n)}{\langle \Phi_0 | \Phi_0 \rangle}, \quad (53)$$

where \mathbf{k} is the momentum transfer between the final and initial momentum of the nucleus, ω is the energy transfer between the final and initial energy of the nucleus, (k, ω) is the four-momentum carried by the virtual photon [31] which is exchanged between the electron and the nucleus, E_n is eigenenergy of the excited states $|\Phi_n\rangle$, and the $\rho(\mathbf{k})$ is the coupling operator.

The response function $S(k, \omega)$ is useful because it is related with the scattering cross section and therefore directly connects theory and experiment. For different scattering processes the couplings of the probe to the nucleus give different $\rho(\mathbf{k})$ operators. Here we calculate the Euclidean response function $E(k, \tau)$ which is related by $S(k, \omega)$ by the Laplace transform,

$$\begin{aligned} E(k, \tau) &= \int_0^\infty e^{-\tau(\omega - \omega_{qe})} S(k, \omega) d\omega \\ &= \frac{e^{\omega_{qe}\tau} \langle \Psi_T | e^{-H\tau_1} [\rho^\dagger(\mathbf{k}) e^{-H\tau} \rho(\mathbf{k})] e^{-H\tau_1} | \Psi_T \rangle}{\langle \Psi_T | e^{-H\tau_1} e^{-H\tau} e^{-H\tau_1} | \Psi_T \rangle}, \end{aligned} \quad (54)$$

where $\omega_{qe} = k^2/2m$ and τ_1 is chosen to be large enough to project out the ground state Φ_0 from the trial wave function Ψ_T .

The problem of analytically continuing from $S(k, \omega)$ from $E(k, \tau)$ by inverting the Laplace transform is numerically unstable, but various methods have made progress [30, 32].

In diffusion QMC such as GFMC and AFDMC, it is often $\langle \Psi_T | \rho^\dagger(\mathbf{k}) e^{-H\tau} \rho(\mathbf{k}) | \Phi_0 \rangle$ that is calculated. Since the operator $\rho^\dagger(\mathbf{k}) e^{-H\tau} \rho(\mathbf{k})$ does not commute with the Hamiltonian, $\langle \Psi_T | \rho^\dagger(\mathbf{k}) e^{-H\tau} \rho(\mathbf{k}) | \Phi_0 \rangle$ is a mixed estimator (although forward walking can improve this) instead of the true ground-state estimator $\langle \Phi_0 | \rho^\dagger(\mathbf{k}) e^{-H\tau} \rho(\mathbf{k}) | \Phi_0 \rangle$. Using PIMC, the response function calculation is straightforward.

We calculate the ^4He Euclidean response functions that correspond to several single-nucleon couplings of $\rho(\mathbf{k})$ which are similar with those calculated in Ref. [13]. These include the nucleon coupling $\rho_N(\mathbf{k})$, proton coupling $\rho_p(\mathbf{k})$, isovector coupling $\rho_\tau(\mathbf{k})$, spin-longitudinal coupling $\rho_{\sigma\tau L}(\mathbf{k})$ and spin-transverse coupling $\rho_{\sigma\tau T}(\mathbf{k})$. They are defined as

$$\rho_N(\mathbf{k}) = \sum_{i=1}^A e^{i\mathbf{k}\cdot\mathbf{r}_i}, \quad (55)$$

$$\rho_p(\mathbf{k}) = \sum_{i=1}^A e^{i\mathbf{k}\cdot\mathbf{r}_i} \frac{1 + \tau_{iz}}{2}, \quad (56)$$

$$\rho_\tau(\mathbf{k}) = \sum_{i=1}^A e^{i\mathbf{k}\cdot\mathbf{r}_i} \tau_{iz}, \quad (57)$$

$$\rho_{\sigma\tau L}(\mathbf{k}) = \sum_{i=1}^A e^{i\mathbf{k}\cdot\mathbf{r}_i} (\boldsymbol{\sigma}_i \cdot \hat{\mathbf{k}}) \tau_{iz}, \quad (58)$$

$$\rho_{\sigma\tau T}(\mathbf{k}) = \sum_{i=1}^A e^{i\mathbf{k}\cdot\mathbf{r}_i} (\boldsymbol{\sigma}_i \times \hat{\mathbf{k}}) \tau_{iz}, \quad (59)$$

where \mathbf{r}_i is the position of particle i . Since the ground state of ^4He has total isospin and its z component both 0, and it is a spherically symmetric object, the response functions do not depend on the direction of \mathbf{k} . When calculating the $E(k, \tau)$, the momentum \mathbf{k} can be averaged over all the directions.

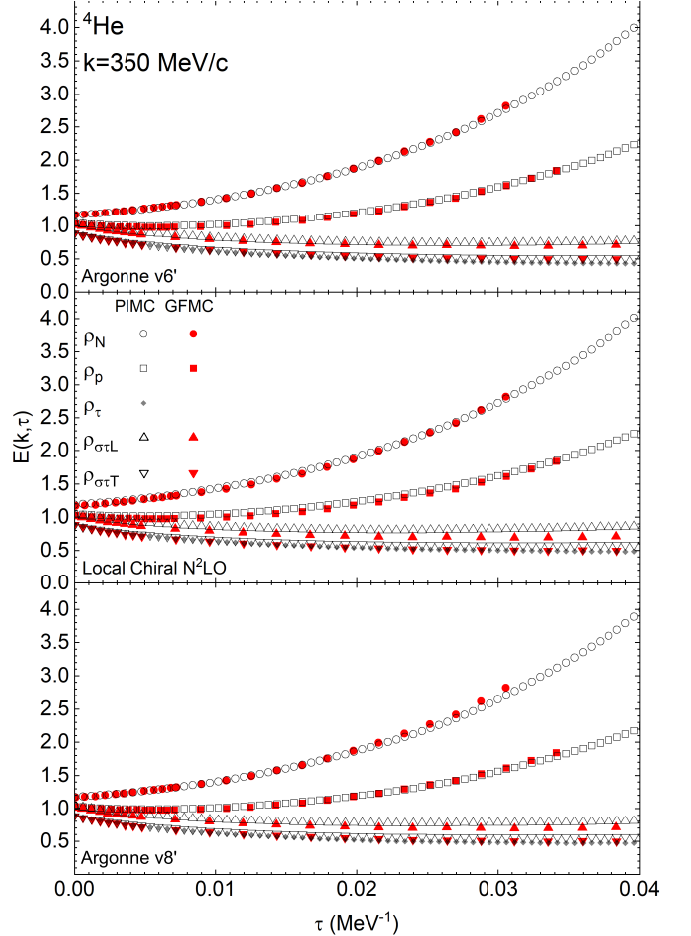


FIG. 9. Angle averaged response functions $E_\alpha(k, \tau)$ of ^4He at $k = 350$ MeV/c based for AV6', local chiral $N^2\text{LO}$, and AV8' interactions. GFMC results [13] is based on the AV8' plus the Urbana model-VIII interactions. The error bar of $E_\alpha(k, \tau)$ at each point is not plotted since it is smaller than the size of the corresponding symbol.

Figure 9 for AV6', local chiral $N^2\text{LO}$, and AV8' interactions shows all of the angle-averaged Euclidean response functions E_α for the corresponding ρ_α defined above. Each of E_α has been normalized such that $\lim_{k \rightarrow \infty} E_\alpha(k, \tau = 0) = 1$. The red dots are digitized from the Fig.3 in Ref. [13] based on GFMC calculations, so that we can compare our results with theirs. Clearly our results are compara-

ble with theirs. The small differences between ours and theirs comes from several sources. First, we use PIMC which require no forward walking, they use GFMC which requires forward walking. Second, the interactions are not exactly the same, they used the Argonne $v8$ interaction combined with the Urbana model-VIII. Third, we use τ_{iz} in stead of $\tau_+(i)$ for the isovector, spin-longitudinal, and spin-transverse couplings; this is suggested in their paper when dealing with an isoscalar target like the ground state ${}^4\text{He}$ and with interactions that conserve the number of protons and neutrons.

E. Computational scaling

Overall, for PIMC, the scaling of required computational time with the number of nucleons and the number of time slices are comparable with those for GFMC with a somewhat larger prefactor. PIMC calculations for propagating a short time step are the same as GFMC and scale with the number of spin/isospin states $N_{\text{tot}} = \frac{A!}{Z!(A-Z)!} 2^A$ if isospin breaking terms are included in the propagation.

The path integral requires additional updates of the whole path when new path positions are included which are absent in GFMC. We expect these to scale with the path length. But typically require less than an order of magnitude of additional computations for the sampling methods we have used.

In order to take advantage of the ability to calculate operator expectations in the middle of the path, PIMC typically needs twice the total imaginary time required to converge the energy.

An advantage of the path-integral method is that because of the Metropolis sampling, the time-step errors even for the simplest short-time propagator can be readily controlled. We can extrapolate to the zero time-step limit using larger time steps than GFMC. That is, in a typical GFMC calculation, an approximate propagator is sampled, and the ratio of the correct propagator at the sampled position and the approximation is included in a weight. In the path integral version instead of this weight, the Metropolis accept/reject step is used. This replaces the fluctuating weight, with its attendant increase in variance with Metropolis rejections. In our formalism, rejections are inexpensive, with the result that we find much lower variance for larger time steps, and can therefore take larger time steps and still extrapolate to the zero time-step limit.

The calculation here use very simple trial wave functions in order to show the convergence for a variety of expectation values and responses. Much better trial functions are typically used in GFMC calculations. These will improve our convergence and lower variances.

GFMC calculations typically use a pair-product propagator. Its use in the path integral calculation is straightforward and it would be used for heavier nuclei. We expect that this would allow even larger time steps and more efficient calculations.

Overall, by using larger steps, better trial wave functions, pair-product propagator, we expect the PIMC scaling to be similar to GFMC, with total calculation times essentially proportional to 4^A .

VI. SUMMARY AND OUTLOOK

By using a variety of sampling techniques along with the optimized strategies of calculating and updating the path we successfully performed real-space accurate ground-state nuclear PIMC calculation of light nuclei, based on local chiral with $N^2\text{LO}$, $\text{AV6}'$, and $\text{AV8}'$ interactions. From our analysis in Sec. V A we can conclude that our choices of total imaginary time indeed projected out the ground states. Also, the extrapolation behavior between $\langle \hat{O} \rangle$ and $\langle \hat{O}(\Delta\tau) \rangle$ are as expected. As discussed in Sec. II E, we verified the expected path discretization errors and extrapolated the results to zero time-step error. These results show that the nuclear PIMC method is accurate and reliable.

Our PIMC ground-state energies of light nuclei are consistent with the results from GFMC and AFDMC as shown in Tables I, II and III. For operators which do not commute with Hamiltonian and cannot be obtained from diffusion Monte Carlo based methods such GFMC and AFDMC without forward walking, we easily get reliable results. We calculated accurate particle number density distributions $\rho(r)$, RMS radii, and the angle-averaged Euclidean response functions.

These results show the power of real-space PIMC calculation for light nuclei. In our PIMC calculation, we find that even with our simple Trotter break up of the propagator, a time step of $10^{-4} - 10^{-3} \text{ MeV}^{-1}$ works reasonably well. Depending on τ and $\Delta\tau$, the number of beads for PIMC ranges from 41 to 3001. In the most time consuming case, such as the $\text{AV8}'$ interaction for $\tau = 0.3 \text{ MeV}^{-1}$ and $\Delta\tau = 10^{-4} \text{ MeV}^{-1}$, we need 3000 short-time propagators and therefore 3001 beads. Such a calculation, to reach a less than 0.02 MeV error in the ground-state energy calculation, takes about 40000 core hours for the interactions used. Results with 41 beads only take a few hundred core hours.

Our calculations here are for $A \leq 4$. For $A > 4$, GFMC has a serious fermion sign/phase problem, and our path integral calculations will as well. Initially for such calculations we expect to be able to use constrained path methods as in GFMC calculations[15] or as in finite-temperature path-integral calculations[1]. These can be either based on the trial wave-function phase as in GFMC or from the trial wave function at the ends and the propagator as in some constrained path-integral methods. One advantage to the path-integral formalism is that, unlike GFMC, we can have an upper-bound principle for all of these constraints if we calculate the expectation value of the Hamiltonian at the center of the path with equivalent constraints on the left and right paths. This can open up the possibilities of optimizing both the trial functions and the constraints

within the path-integral method.

Our ^4He calculations here are a benchmark test for future PIMC calculations of larger nuclei. We also believe that, based on what we have in this paper, a nuclear PIMC finite-temperature calculation of α particles or neutron matter are feasible. Three-body interactions can be readily included in a straightforward manner to perform more accurate PIMC calculations.

ACKNOWLEDGMENTS

We thank professor Francesco Pederiva for helpful discussions. This work was supported by the National Science Foundation Grant No. PHY-1404405. We acknowledge Research Computing at Arizona State University for providing HPC and storage resources that have contributed to the research results reported within this paper. All calculations were performed on the Agave research computing cluster.

Appendix A: Path Calculation

The $A_{lr}(\mathcal{R})$ and $B_{lr}(\mathcal{R})$ in Eq. (35) are real functions,

$$A_{lr}(\mathcal{R}) = \frac{\text{Re}[g(\mathcal{R})_{lr}]}{|\text{Re}[f(\mathcal{R})_{lr}]|}, \quad (\text{A1})$$

$$B_{lr}(\mathcal{R}) = \frac{\text{Re}[f(\mathcal{R})_{lr}]}{|\text{Re}[f(\mathcal{R})_{lr}]|}, \quad (\text{A2})$$

$P_{lr}(\mathcal{R})$ in Eq. (35) is the probability distribution,

$$P_{lr}(\mathcal{R}) = \frac{|\text{Re}[f(\mathcal{R})_{lr}]|}{\mathcal{N}}, \quad (\text{A3})$$

which is normalized, $\sum_l \sum_r \int d\mathcal{R} P_{lr}(\mathcal{R}) = 1$. The normalization factor $\mathcal{N} = \sum_l \sum_r \int d\mathcal{R} |\text{Re}[f(\mathcal{R})_{lr}]|$ cancels in the Metropolis algorithm implementation.

Function $f(\mathcal{R})_{lr}$ comes from the denominator of Eq. (34) and it does not depend on where the operator \hat{O} is placed. Function $g(\mathcal{R})_{lr}$ comes from the numerator of Eq. (34), and it depends on which bead M the operator \hat{O} is placed at. They can be written as

$$f(\mathcal{R})_{lr} = f_{lr}^V(\mathcal{R})g^F(\mathcal{R}), \quad (\text{A4})$$

$$g(\mathcal{R})_{lr} = g_{lr,M}^V(\mathcal{R})g^F(\mathcal{R}). \quad (\text{A5})$$

Function $g^F(\mathcal{R})$ in Eqs. (A4)–(A5) is

$$g^F(\mathcal{R}) = \prod_{I=0}^{N-1} G_{I,I+1}^f. \quad (\text{A6})$$

The Gaussian free particle propagator, $G_{I,I+1}^f$ is defined in Eq.(26) and connects beads R_I and R_{I+1} . The product $\prod_{I=0}^{N-1} G_{I,I+1}^f$ in the functions $A_{lr}(\mathcal{R})$ and $B_{lr}(\mathcal{R})$, cancels. They become

$$A_{lr}(\mathcal{R}) = \frac{\text{Re}[g_{lr,M}^V(\mathcal{R})]}{|\text{Re}[f_{lr}^V(\mathcal{R})]|}, \quad (\text{A7})$$

$$B_{lr}(\mathcal{R}) = \frac{\text{Re}[f_{lr}^V(\mathcal{R})]}{|\text{Re}[f_{lr}^V(\mathcal{R})]|}. \quad (\text{A8})$$

To simplify the notations in the expressions of functions $g_{lr,M}^V(\mathcal{R})$ and $f_{lr}^V(\mathcal{R})$, we define states $|\psi_M^r(\mathcal{R})\rangle$ and $|\psi_M^l(\mathcal{R})\rangle$ where the Dirac notation is used for the spin/isospin states, while the position parts of the wave function are evaluated at the bead positions given by \mathcal{R} ,

$$|\psi_M^r(\mathcal{R})\rangle \equiv \begin{cases} \sum_S U_V(R_M, \frac{\Delta\tau}{2})U_V^\dagger(R_M, \frac{\Delta\tau}{2})\mathcal{G}(R_M, R_{M+1})U_V(R_{M+1}, \frac{\Delta\tau}{2})U_V^\dagger(R_{M+1}, \frac{\Delta\tau}{2})\mathcal{G}(R_M, R_{M+2})\dots \\ \quad \dots U_V^\dagger(R_{N-1}, \frac{\Delta\tau}{2})\mathcal{G}(R_{N-1}, R_N)U_V(R_N, \frac{\Delta\tau}{2})|S\rangle\langle R_N S|\psi_T^r\rangle, & (M \neq N, 0) \\ \sum_S U_V(R_N, \frac{\Delta\tau}{2})|S\rangle\langle R_N S|\psi_T^r\rangle, & (M = N) \\ \sum_S U_V^\dagger(R_0, \frac{\Delta\tau}{2})\mathcal{G}(R_0, R_1)U_V(R_1, \frac{\Delta\tau}{2})U_V^\dagger(R_1, \frac{\Delta\tau}{2})\mathcal{G}(R_1, R_2)U_V(R_2, \frac{\Delta\tau}{2})U_V^\dagger(R_2, \frac{\Delta\tau}{2})\mathcal{G}(R_2, R_3)\dots \\ \quad \dots U_V^\dagger(R_{N-1}, \frac{\Delta\tau}{2})\mathcal{G}(R_{N-1}, R_N)U_V(R_N, \frac{\Delta\tau}{2})|S\rangle\langle R_N S|\psi_T^r\rangle. & (M = 0) \end{cases} \quad (\text{A9})$$

$$|\psi_M^l(\mathcal{R})\rangle \equiv \begin{cases} \sum_S U_V(R_M, \frac{\Delta\tau}{2})U_V^\dagger(R_M, \frac{\Delta\tau}{2})\mathcal{G}^*(R_M, R_{M-1})U_V(R_{M-1}, \frac{\Delta\tau}{2})U_V^\dagger(R_{M-1}, \frac{\Delta\tau}{2})\mathcal{G}^*(R_{M-1}, R_{M-2})\dots \\ \dots \mathcal{G}^*(R_2, R_1)U_V(R_1, \frac{\Delta\tau}{2})U_V^\dagger(R_1, \frac{\Delta\tau}{2})\mathcal{G}^*(R_1, R_0)U_V(R_0, \frac{\Delta\tau}{2})|S\rangle\langle R_0S|\psi_T^l\rangle, & (M \neq 0, N) \\ \sum_S U_V(R_0, \frac{\Delta\tau}{2})|S\rangle\langle R_0S|\psi_T^l\rangle, & (M = 0) \\ \sum_S U_V^\dagger(R_N, \frac{\Delta\tau}{2})\mathcal{G}^*(R_N, R_{N-1})U_V(R_{N-1}, \frac{\Delta\tau}{2})U_V^\dagger(R_{N-1}, \frac{\Delta\tau}{2})\mathcal{G}^*(R_{N-1}, R_{N-2})U_V(R_{N-2}, \frac{\Delta\tau}{2})\dots \\ \dots \mathcal{G}^*(R_2, R_1)U_V(R_1, \frac{\Delta\tau}{2})U_V^\dagger(R_1, \frac{\Delta\tau}{2})\mathcal{G}^*(R_1, R_0)U_V(R_0, \frac{\Delta\tau}{2})|S\rangle\langle R_0S|\psi_T^l\rangle. & (M = N) \end{cases} \quad (\text{A10})$$

Note that for AV6' which does not have spin-orbit term, the $\mathcal{G}(R, R')$ factors are 1.

Both $|\psi_M^l(\mathcal{R})\rangle$ and $|\psi_M^r(\mathcal{R})\rangle$ can be written in the A -particle spin-isospin basis $|S\rangle$ such that

$$|\psi_M^r(\mathcal{R})\rangle = \sum_S |S\rangle\langle S|\psi_M^r(\mathcal{R})\rangle = \sum_S \phi_M^r(\mathcal{R}, S)|S\rangle, \quad (\text{A11})$$

$$|\psi_M^l(\mathcal{R})\rangle = \sum_S |S\rangle\langle S|\psi_M^l(\mathcal{R})\rangle = \sum_S \phi_M^l(\mathcal{R}, S)|S\rangle, \quad (\text{A12})$$

where $\phi_M^r(\mathcal{R}, S)$ and $\phi_M^l(\mathcal{R}, S)$ are the corresponding probability amplitude.

The function $g_{lr,M}^V(\mathcal{R})$ depends on which bead, M , the operator \hat{O} is placed. For a given M , with the defined $|\psi_M^r(\mathcal{R})\rangle$ and $|\psi_M^l(\mathcal{R})\rangle$, it is

$$g_{lr,M}^V(\mathcal{R}) = \begin{cases} \langle \psi_{M-1}^l(\mathcal{R})|\mathcal{G}(R_{M-1}, R_M)U_V(R_M, \frac{\Delta\tau}{2})\hat{O}U_V^\dagger(R_M, \frac{\Delta\tau}{2})\mathcal{G}(R_M, R_{M+1})|\psi_{M+1}^r(\mathcal{R})\rangle, & (M \neq 0, N) \\ \sum_S \langle \psi_T^l|\hat{O}|R_0S\rangle\langle S|\psi_0^r(\mathcal{R})\rangle, & (M = 0) \\ \sum_S \langle \psi_N^l(\mathcal{R})|S\rangle\langle R_NS|\hat{O}|\psi_T^r\rangle. & (M = N) \end{cases} \quad (\text{A13})$$

The integer M in $g_{lr}^V(\mathcal{R})$ is usually set so that \hat{O} operates at the central bead. This guarantees that the calculation gives the ground-state expectation value of \hat{O} if the total imaginary time τ is large.

If the operator \hat{O} commutes with Hamiltonian, then it is often convenient to calculate \hat{O} by operating on the trial wave function. The corresponding $g(\mathcal{R})_{lr}$ can be calculated as,

$$g(\mathcal{R})_{lr} = \frac{[g_{lr,M}^V(\mathcal{R})|_{M=0} + g_{lr,M}^V(\mathcal{R})|_{M=N}]}{2} g^F(\mathcal{R}). \quad (\text{A14})$$

This is for example how we calculate the ground-state energy $\hat{O} = H$.

The function $f_{lr}^V(\mathcal{R})$ does not depend on M . Its value is the same as long as the left and right orders l, r , and \mathcal{R} are the same. For any integer M ranges from 0 to $N-1$, it is calculated as

$$\begin{aligned} f_{lr}^V(\mathcal{R}) &= \langle \psi_M^l(\mathcal{R})|\mathcal{G}(R_M, R_{M+1})|\psi_{M+1}^r(\mathcal{R})\rangle \\ &= \sum_S \langle \psi_M^l(\mathcal{R})|S\rangle\langle S|\mathcal{G}(R_M, R_{M+1})|\psi_{M+1}^r(\mathcal{R})\rangle. \end{aligned} \quad (\text{A15})$$

Appendix B: Path Updating

Based on Eq.(A9) and Eq.(A10) we write recursion relations

$$|\psi_M^r(\mathcal{R})\rangle = \begin{cases} \sum_S U_V(R_M, \frac{\Delta\tau}{2})U_V^\dagger(R_M, \frac{\Delta\tau}{2})\mathcal{G}(R_M, R_{M+1})|S\rangle\langle S|\psi_{M+1}^r(\mathcal{R})\rangle, & (M \neq N, 0) \\ \sum_S U_V(R_N, \frac{\Delta\tau}{2})|S\rangle\langle R_NS|\psi_T^r\rangle, & (M = N) \\ \sum_S U_V^\dagger(R_0, \frac{\Delta\tau}{2})\mathcal{G}(R_0, R_1)|S\rangle\langle S|\psi_1^r(\mathcal{R})\rangle, & (M = 0) \end{cases} \quad (\text{B1})$$

$$|\psi_M^l(\mathcal{R})\rangle = \begin{cases} \sum_S U_V(R_M, \frac{\Delta\tau}{2}) U_V^\dagger(R_M, \frac{\Delta\tau}{2}) \mathcal{G}^*(R_M, R_{M-1}) |S\rangle \langle S| \psi_{M-1}^l(\mathcal{R})\rangle, & (M \neq 0, N) \\ \sum_S U_V(R_0, \frac{\Delta\tau}{2}) |S\rangle \langle R_0 S| \psi_T^l, & (M = 0) \\ \sum_S U_V^\dagger(R_N, \frac{\Delta\tau}{2}) \mathcal{G}^*(R_N, R_{N-1}) |S\rangle \langle S| \psi_{N-1}^l(\mathcal{R})\rangle. & (M = N) \end{cases} \quad (\text{B2})$$

We then directly calculate $|\psi_{N-1}^r(\mathcal{R})\rangle$ from $|\psi_N^r(\mathcal{R})\rangle$, then $|\psi_{N-2}^r(\mathcal{R})\rangle$ from $|\psi_{N-1}^r(\mathcal{R})\rangle$, \dots , until $|\psi_{M+1}^r(\mathcal{R})\rangle$ from $|\psi_{M+2}^r(\mathcal{R})\rangle$ from right to left. Similarly we calculate all of the $|\psi_M^l(\mathcal{R})\rangle$ from $|\psi_{M-1}^l(\mathcal{R})\rangle$.

Once we have the corresponding $|\psi_M^r(\mathcal{R})\rangle$ and $|\psi_M^l(\mathcal{R})\rangle$, we use Eqs. (A15) and (A13) to calculate $f_{lr}^V(\mathcal{R})$ and $g_{lr,M}^V(\mathcal{R})$ and then $A_{lr}(\mathcal{R})$ and $B_{lr}(\mathcal{R})$ and thus $\langle \hat{O}(\Delta\tau) \rangle$. This recursive updating strategy for $|\psi_M^r(\mathcal{R})\rangle$ and $|\psi_M^l(\mathcal{R})\rangle$ is efficient when updating part of the path.

-
- [1] D. M. Ceperley, *Reviews of Modern Physics* **67**, 279 (1995).
[2] A. Sarsa, K. E. Schmidt, and W. R. Magro, *Journal of Chemical Physics* **113**, 1366 (2000).
[3] S. Baroni and S. Moroni, *Physical Review Letters* **82**, 4745 (1999).
[4] J. Carlson, *Physical Review C* **36**, 2026 (1987).
[5] K. Schmidt and S. Fantoni, *Physics Letters B* **446**, 99 (1999).
[6] K. J. Runge, *Physical Review B* **45**, 7229 (1992).
[7] J. Casulleras and J. Boronat, *Physical Review B* **52**, 3654 (1995).
[8] M. Samaras and C. J. Hamer, *Australian Journal of Physics* **52**, 637 (1999).
[9] A. Gezerlis, I. Tews, E. Epelbaum, M. Freunek, S. Gandolfi, K. Hebeler, A. Nogga, and A. Schwenk, *Physical Review C* **90**, 054323 (2014).
[10] J. E. Lynn, I. Tews, J. Carlson, S. Gandolfi, A. Gezerlis, K. E. Schmidt, and A. Schwenk, *Physical Review C* **96**, 054007 (2017).
[11] D. Lonardonì, S. Gandolfi, J. E. Lynn, C. Petrie, J. Carlson, K. E. Schmidt, and A. Schwenk, *Physical Review C* **97**, 044318 (2018).
[12] R. B. Wiringa and S. C. Pieper, *Physical Review Letters* **89**, 182501 (2002).
[13] J. Carlson and R. Schiavilla, *Physical Review C* **49**, R2880 (1994).
[14] J. Carlson and R. B. Wiringa, in *Computational Nuclear Physics 1: Nuclear Structure*, edited by K. Langanke, J. A. Maruhn, and S. E. Koonin (Springer-Verlag, 1991) Chap. 9, pp. 171–187.
[15] J. Carlson, S. Gandolfi, F. Pederiva, S. C. Pieper, R. Schiavilla, K. E. Schmidt, and R. B. Wiringa, *Reviews of Modern Physics* **87**, 1067 (2015).
[16] J. Lomnitz-Adler, V. Pandharipande, and R. Smith, *Nuclear Physics A* **361**, 399 (1981).
[17] K. E. Schmidt and M. A. Lee, *Physical Review E* **51**, 5495 (1995).
[18] N. Hatano and M. Suzuki, *Physics Letters A* **153**, 191 (1991).
[19] R. Chen, *Path Integral Quantum Monte Carlo Method for Light Nuclei*, Ph.D. thesis, Arizona State University (2020), <https://arxiv.org/abs/2207.07246>.
[20] N. Metropolis, A. W. Rosenbluth, M. N. Rosenbluth, A. H. Teller, and E. Teller, *Journal of Chemical Physics* **21**, 1087 (1953).
[21] B. L. Hammond, W. A. Lester, and P. J. Reynolds, *Monte Carlo Methods in Ab Initio Quantum Chemistry* (WORLD SCIENTIFIC, 1994).
[22] G. Carleo, F. Becca, S. Moroni, and S. Baroni, *Physical Review E* **82**, 046710 (2010).
[23] J. E. Lynn, J. Carlson, E. Epelbaum, S. Gandolfi, A. Gezerlis, and A. Schwenk, *Physical Review Letters* **113**, 192501 (2014).
[24] D. Lee, *Frontiers in Physics* **8**, 174 (2020).
[25] Wikipedia contributors, Nuclear binding energy — Wikipedia, the free encyclopedia, https://en.wikipedia.org/w/index.php?title=Nuclear_binding_energy&oldid=957017239 (2020), [Online; accessed 10-July-2020].
[26] J. Lynn, I. Tews, S. Gandolfi, and A. Lovato, *Annual Review of Nuclear and Particle Science* **69**, 279 (2019), <https://doi.org/10.1146/annurev-nucl-101918-023600>.
[27] J. Carlson and R. Schiavilla, *Physical Review Letters* **68**, 3682 (1992).
[28] J. Carlson, J. Jourdan, R. Schiavilla, and I. Sick, *Physical Review C* **65**, 024002 (2002).
[29] A. Lovato, S. Gandolfi, R. Butler, J. Carlson, E. Lusk, S. C. Pieper, and R. Schiavilla, *Physical Review Letters* **111**, 092501 (2013).
[30] A. Lovato, S. Gandolfi, J. Carlson, S. C. Pieper, and R. Schiavilla, *Physical Review C* **91**, 062501 (2015).
[31] S. Bacca and S. Pastore, *Journal of Physics G: Nuclear and Particle Physics* **41**, 123002 (2014).
[32] G. Shen, L. E. Marcucci, J. Carlson, S. Gandolfi, and R. Schiavilla, *Physical Review C* **86**, 035503 (2012).